

Central Lancashire Online Knowledge (CLOK)


Title	Constructing long-cycling crystalline C ₃ N ₄ -based carbonaceous anodes for sodium-ion battery via N configuration control
Type	Article
URL	https://clock.uclan.ac.uk/id/eprint/48530/
DOI	https://doi.org/10.1002/cey2.388
Date	2023
Citation	Wang, Ying, Li, Hongguan, Di, Shuanlong, Zhai, Boyin, Niu, Ping, Kelarakis, Antonios, Wang, Shulan and Li, Li (2023) Constructing long-cycling crystalline C ₃ N ₄ -based carbonaceous anodes for sodium-ion battery via N configuration control. Carbon Energy.
Creators	Wang, Ying, Li, Hongguan, Di, Shuanlong, Zhai, Boyin, Niu, Ping, Kelarakis, Antonios, Wang, Shulan and Li, Li

It is advisable to refer to the publisher's version if you intend to cite from the work.
<https://doi.org/10.1002/cey2.388>

For information about Research at UCLan please go to <http://www.uclan.ac.uk/research/>

All outputs in CLOK are protected by Intellectual Property Rights law, including Copyright law. Copyright, IPR and Moral Rights for the works on this site are retained by the individual authors and/or other copyright owners. Terms and conditions for use of this material are defined in the <http://clock.uclan.ac.uk/policies/>

Constructing long-cycling crystalline C₃N₄-based carbonaceous anodes for sodium-ion battery via N configuration control

Ying Wang^{1,2} | Hongguan Li^{1,2} | Shuanlong Di³ | Boyin Zhai³ | Ping Niu^{1,2} | Antonios Kelarakis⁴ | Shulan Wang³ | Li Li^{1,2,5} 

¹School of Metallurgy, Northeastern University, Shenyang, Liaoning, China

²State Key Laboratory of Rolling and Automation, Northeastern University, Shenyang, Liaoning, China

³Department of Chemistry, College of Science, Northeastern University, Shenyang, Liaoning, China

⁴School of Natural Sciences, UCLan Research Centre for Smart Materials, University of Central Lancashire, Preston, UK

⁵Foshan Graduate School of Innovation, Northeastern University, Foshan, Guangdong, China

Correspondence

Li Li, School of Metallurgy, Northeastern University, Shenyang 110819, Liaoning, China.

Email: lilicmu@alumni.cmu.edu

Funding information

National Natural Science Foundation of China, Grant/Award Number: 51904059; Applied Basic Research Program of Liaoning, Grant/Award Number: 2022JH2/101300200; Guangdong Basic and Applied Basic Research Foundation, Grant/Award Number: 2022A1515140188; Fundamental Research Funds for the Central Universities, Grant/Award Numbers: N2002005, N2125004, N2225044

Abstract

Carbon nitrides with two-dimensional layered structures and high theoretical capacities are attractive as anode materials for sodium-ion batteries while their low crystallinity and insufficient structural stability strongly restrict their practical applications. Coupling carbon nitrides with conductive carbon may relieve these issues. However, little is known about the influence of nitrogen (N) configurations on the interactions between carbon and C₃N₄, which is fundamentally critical for guiding the precise design of advanced C₃N₄-related electrodes. Herein, highly crystalline C₃N₄ (poly (triazine imide), PTI) based all-carbon composites were developed by molten salt strategy. More importantly, the vital role of pyrrolic-N for enhancing charge transfer and boosting Na⁺ storage of C₃N₄-based composites, which was confirmed by both theoretical and experimental evidence, was spot-highlighted for the first time. By elaborately controlling the salt composition, the composite with high pyrrolic-N and minimized graphitic-N content was obtained. Profiting from the formation of highly crystalline PTI and electrochemically favorable pyrrolic-N configurations, the composite delivered an unusual reverse growth and record-level cycling stability even after 5000 cycles along with high reversible capacity and outstanding full-cell capacity retention. This work broadens the energy storage applications of C₃N₄ and provides new prospects for the design of advanced all-carbon electrodes.

KEYWORDS

anode, highly crystalline C₃N₄, N configuration, sodium-ion batteries, ultra-long cyclic stability

1 | INTRODUCTION

The development of advanced energy storage technologies is of significance in realizing large-scale utilization of sustainable energy, especially with the recent rising concerns about supply issues of fossil fuels and their environmental problems.^{1–4} Different from lithium-ion batteries (LIBs) that need unevenly distributed lithium resources, sodium-ion batteries (SIBs) with abundant sodium natural reserves are viewed as promising alternative energy storage devices.^{5–8} However, the electrochemical performance of SIBs is strongly influenced by available anode materials while the graphite anode commonly used in LIBs is generally viewed as ineffective for high-performance SIBs considering the formation of thermodynamically unstable Na-graphite compounds.^{9,10} Nevertheless, carbonaceous materials are still preferred for the commercialization of SIBs considering their low expenses and environmentally benign nature.^{11,12} The commonly studied carbonaceous anodes including hard carbon, graphene, carbon fiber, or expanded graphite still suffer from issues such as low practical capacity, huge volume changes, and poor cycling stability. Therefore, it is still challenging to develop high-performance all-carbon anode materials with rapid Na^+ storage capability and long cycle lifespan.

As a new type of two-dimensional layered nitrogen-containing carbon-based materials, graphitic carbon nitride ($\text{g-C}_3\text{N}_4$) has presented growing potential in the energy storage field lately owing to its merits of low cost, variable modulation, high theoretical capacity, and facile synthesis.^{13–15} However, its poor electronic conductivity and severe structural collapse during intercalation/deintercalation have strongly restricted its usage as SIBs anodes.¹⁶ Meanwhile, the crystallinity decrease induced by partially reacting with alkali metal ions also leads to inferior stability and low capacity.¹⁷ Coupling with conductive carbon is viewed as one of the attractive strategies to offset the drawbacks of $\text{g-C}_3\text{N}_4$ by promoting its structural durability and electronic conductivity. For instance, fullerene intercalated carbon nitride ($\text{C}_{60}@\text{CN}$) composites showed expanded interlayer spacing and increased charge transfer rate due to the introduction of fullerene as a conductive spacer.¹⁸ Despite the encouraging research progress initiated for improving the sodium storage capability of C_3N_4 , it is still lacking the fundamental understanding for the interactions between C_3N_4 and carbon additives with many unresolved problems remaining. Meanwhile, C_3N_4 reported in most cases shows the melon-based structure, which is viewed as an amorphous or semi-crystalline phase with low in-plane electron conduction and inferior electrochemical activity.¹⁹ Hence, the

detailed investigation for the elaborate control of C_3N_4 /carbon interactions with effective crystallinity enhancement is highly desirable for the rational design of advanced C_3N_4 anodes.

Herein, to validate the influence of nitrogen (N) configurations on the interactions between C_3N_4 and carbon as well as to highlight the role of pyrrolic-N that is not commonly emphasized in previous studies, a composite of N-doped carbon (NC) and highly crystalline C_3N_4 was prepared by one-pot molten salt strategy. Note that different from the commonly studied amorphous C_3N_4 with melon structure synthesized from thermal condensation,²⁰ the crystalline C_3N_4 allotrope poly(triazine imide) (PTI) was introduced through molten salt treatment with the expectation to enhance crystallinity and elevate electrochemical performances. High crystallinity is beneficial for strengthening charge dynamics and accelerating surface charge transport, thereby improving the conductivity of the electrode material. The facile molten salt treatment also achieves the intimate interaction between components with the hierarchical porous structure introduced into composites, all of which are the prerequisites for achieving high sodium storage performances. More importantly, N configurations can be elaborately controlled through molten salt constituents. Compared with ternary salt LiCl/KCl/NaCl , the eutectic binary salt LiCl/KCl with the lower melting point (352°C vs. $450\text{--}500^\circ\text{C}$) is found to better regulate the in-plane polymerization of C_3N_4 and promote the conversion of graphitic-N to pyrrolic-N. Density functional theory (DFT) calculations reveal the superior role of PTI coupled with pyrrolic-N-based carbon over its counterparts, which provides us clues for the rational design of C_3N_4 -based anodes with high sodium adsorption and storage capability. Therefore, the optimized composite electrode showed reverse capacity growth through long-term cycling and delivered a high reversible capacity of 221.2 mAh g^{-1} with a record-level capacity retention of 118.5% over 5000 cycles. The as-prepared anode coupled with commercial-grade cathode also presented excellent full-cell performance.

2 | RESULTS AND DISCUSSION

2.1 | Theoretical calculations

Aiming at the low conductivity and sluggish Na^+ diffusion kinetics of carbon nitrides as the battery materials, herein, we propose a possible solution to enhance their crystallinity by selecting crystalline PTI as the key component in addition to coupling it with conductive NC. Moreover, the detailed interaction

between PTI and NC is worth deep investigation. Meanwhile, to predict the structure and electronic properties for guiding the material design and synthesis, DFT calculations were performed for PTI/NC. Considering the N configuration is of significance to influencing the Na^+ adsorption and diffusion kinetics within the carbon matrix,^{21,22} we put the focus on the study of the interaction between PTI and carbon with different N configurations. The detailed models of PTI/pyrrolic-NC (denoted as PTI/PN) and PTI/graphitic-NC (or quaternary-N, denoted as PTI/QN) were listed in Figures 1A,B, S1, and S2. Furthermore, adsorption models of Na^+ on the surface of PTI/PN and PTI/QN layers (Figures S3 and S4) were also constructed to illustrate the

binding properties with the charge density differences presented in Figure 1C. It can be clearly observed that charge enrichment occurred more uniformly on the isosurface of the PTI/PN layer with high-density charge accumulated, demonstrating stronger interactions between PTI/PN for Na^+ adsorption and charge transfer than that for PTI/QN. The more favorable Na^+ adsorption kinetics for PTI/PN can also be confirmed by its higher adsorption energy (-2.862 eV), which is 7.2 times that for PTI/QN (-0.397 eV) (Figure 1D). The adsorption energies of PTI/QN and PTI/PN on PTI are 2.283 and 1.922 eV (Figure S5), respectively, indicating that Na^+ adsorption on the NC surface is preferred during the electrochemical reaction process. The spatial evolution of electronic states

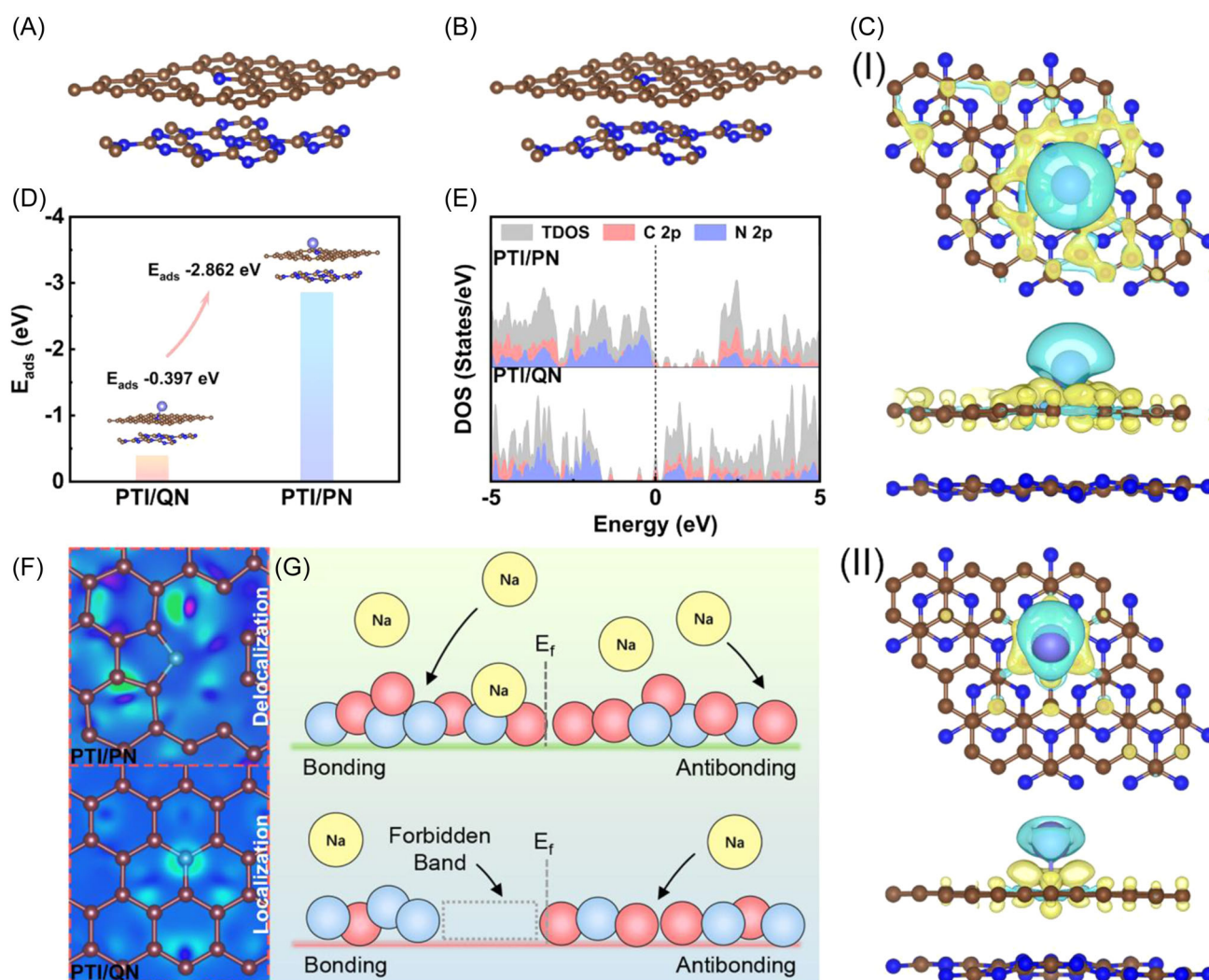


FIGURE 1 DFT calculations of the electronic structure and charge distribution of PTI/carbon composites. Optimized structures of (A) PTI/PN and (B) PTI/QN. The blue and brown balls represent N and C atoms, respectively. (C) Charge density difference of Na^+ adsorption on (I) PTI/PN and (II) PTI/QN. The yellow and cyan regions refer to charge accumulation and depletion, respectively. (D) Adsorption energies of sodium on PTI/QN and PTI/PN (E_{ads} : adsorption energy). (E) The total and partial density of states (TDOS and PDOS) of PTI/PN and PTI/QN. (F) Corresponding two-dimensional projection of charge density contours of PTI/PN and PTI/QN. (G) Schematic diagram of the energy band structures of adsorbed sodium with different N configurations.

at the hetero-interface and interlayer of PTI/PN and PTI/QN jointly dominates the Na^+ adsorption. Further analysis for the spatial evolution of electronic structures reveals that C 2p and N 2p orbital hybridization of PTI/PN shows more concentrated electrons from the low-energy region to the high-energy region, especially near the Fermi level, demonstrating its enhanced density of free electrons and accelerated charge transfer between heterostructure interfaces (Figures 1E and S6). In contrast, the introduction of graphitic-N shifts the density of states to low-energy regions with the appearance of unoccupied bands, which can strongly decrease electron-captured ability and retard Na^+ adsorption (Figures 1E and S7). Meanwhile, the comparison of two-dimensional projection of charge density contours (Figure 1F) shows that electrons are delocalized in the interface of PTI and pyrrolic-N which is more beneficial for charge transfer, while PTI/QN has more localized charges. Consistent with the aforementioned analysis, this result also confirms the more favorable Na^+ adsorption process within PTI/PN than PTI/QN. A schematic diagram was presented in Figure 1G to depict the differences in their electronic structures. The continuous electron distribution of PTI/PN with rapid interfacial reaction kinetics and excellent electron/charge transfer capabilities can effectively promote Na^+ diffusion. Overall, theoretical calculations demonstrate that the favorable Na^+ adsorption kinetics and elevated electronic conductivity within PTI/PN are favorable for achieving high electrochemical performances.

2.2 | Structure and morphology analysis

To achieve the simultaneous formation of crystalline C_3N_4 and efficient compositing between components, a molten salt method was used to obtain the binary molten-salt derived carbon nitride/carbon (BMSCNC) composites in this work (Figure 2A), and the detailed naming convention can be found in Supporting Information. The polymerization process of melamine was elaborately controlled by the molten-salt environment.^{23,24} Herein, binary salts with a lower melting point and better mobility than their ternary counterpart can increase the mass transfer rate for more full condensation, leading to the higher structure order of PTI. Ammonium chloride was used as a sacrificial template to release gases and introduce hierarchical pores, which can solve the issues of low surface area and single pore size distribution that conventional C_3N_4 -related materials encounter.^{25,26} As shown in Figures 2B,C and S8, the as-prepared BMSCNC presented a directional tubular structure with abundant open

channels that are assembled by porous nanosheets in the thickness of 10–15 nm. This structure provides sufficient conductive pathways for fast ion diffusion and efficient electrolyte penetration into the internal surface of active materials, which can also accommodate huge volume changes during cycling.^{27,28} In contrast, ternary molten-salt derived carbon nitride/carbon (TMSCNC) and carbon nitride/carbon (CNC) showed irregular morphology (Figure S9) or even bulk with severe aggregation of particles (Figure S10), which is highly unfavorable for Na^+ storage.^{29–31} The energy-dispersive spectroscopy (EDS) elemental mapping of BMSCNC confirms the homogeneous distribution of C, N, and O through the composite (Figure 2D). Further structural investigation using the transmission electron microscope (TEM) and high-resolution TEM (HRTEM) revealed the ultra-thin multilayer nanosheet of BMSCNC (Figure 2E,F), and the lattice fringe of 0.32 nm was related to (002) crystal plane of triazine-based $\text{g-C}_3\text{N}_4$ that originates from its interlayer stacking (Figure 2G). The TEM results confirm the formation of crystalline C_3N_4 -based carbonaceous composite.

X-ray diffraction patterns were collected to investigate the phase composition of samples (Figure 3A). The primary peak of PTI at around 26.8° is related to the interlayer-stacking of aromatic groups overlapped with the broad peak of turbostratic carbon originating from their π - π interactions.^{32–34} Meanwhile, the peaks in the patterns of BMSCNC and TMSCNC at around 10° are ascribed to the (100) plane of PTI that shifts due to the interaction between carbon and C_3N_4 .¹⁷ The corresponding XRD patterns of $\text{g-C}_3\text{N}_4$ without the addition of carbon were also presented in Figure S11, and PTI was successfully synthesized under molten salt treatment, which is consistent with the previous reports.^{35,36} Moreover, the weakened diffraction peak of 26.8° for PTI treated in binary salt compared with that in ternary salt is due to the multilayer nanosheet stacking of interlayer structure, which agrees with the TEM results shown above.

Fourier-transform infrared (FT-IR) spectra were recorded to further analyze the chemical structures and functional groups of BMSCNC, TMSCNC, and CNC. As shown in Figure 3B, the samples exhibited the structures of carbon nitride and carbon, indicating the successful formation of the composites. The peaks in the range of 1200 – 1700 cm^{-1} represent the stretching mode of CN heterocycles,^{37,38} while the multiple peak signals of CN heterocycles in BMSCNC and TMSCNC were stronger than that of CNC, implying that molten salt promotes the crystallinity of carbon nitride. The peaks at around 810 cm^{-1} can be assigned to the breathing mode of the triazine units.^{39,40} Significantly, compared with TMSCNC

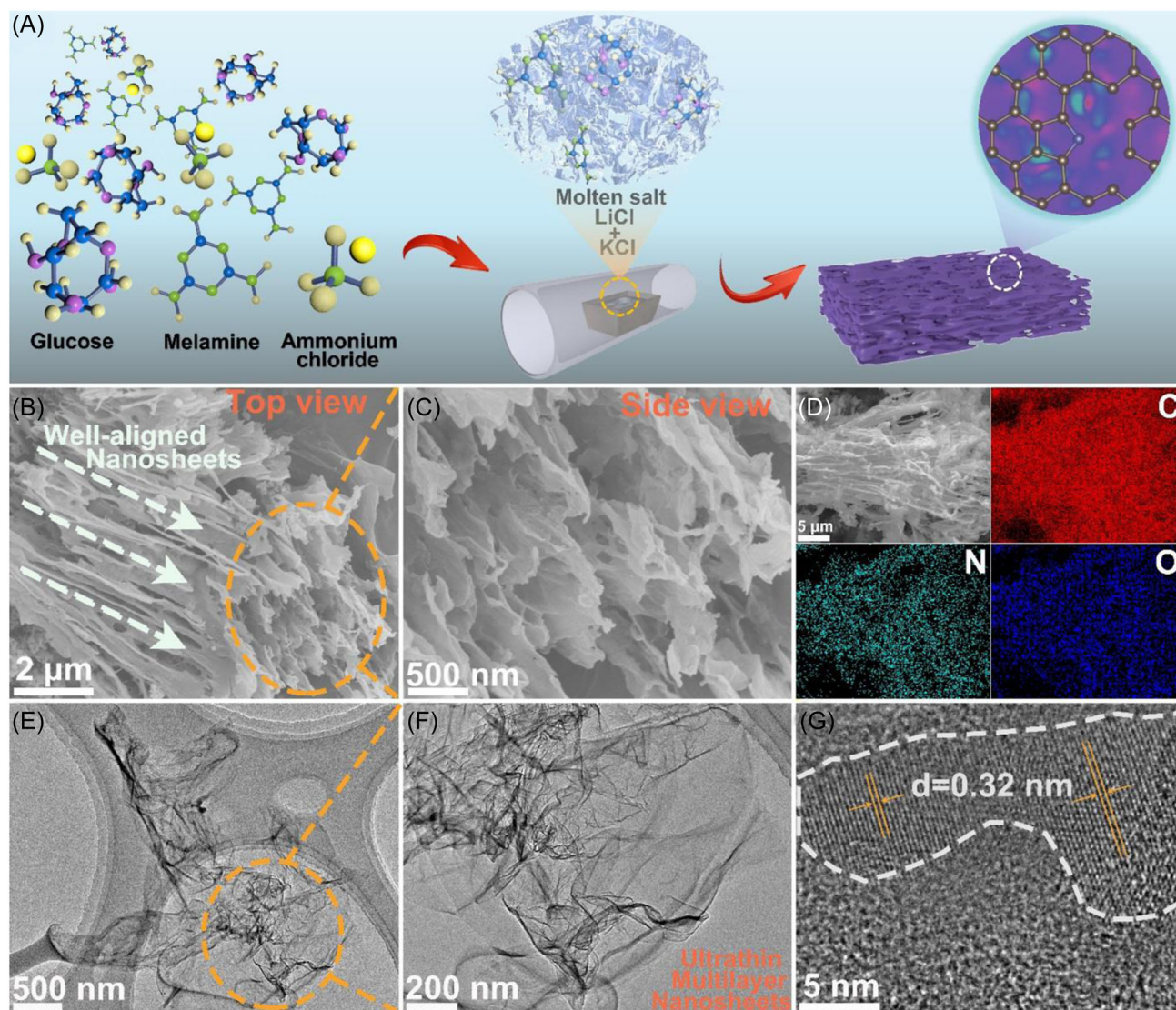


FIGURE 2 Morphology investigation of BMSCNC. (A) Schematic for the formation of BMSCNC through the molten salt protocol. SEM images at (B) low and (C) high magnifications, (D) EDS elemental mappings of C, N, O, (E, F) TEM, and (G) HRTEM images of BMSCNC composite.

and CNC, the intensity of triazine units in BMSCNC was much higher. Moreover, the typical peak of PTI at 640 cm^{-1} was also observed in BMSCNC.⁴¹ The characteristic peaks at 810 and 640 cm^{-1} confirm the high structural order of BMSCNC. Furthermore, the vibration band intensity of $\text{-C}\equiv\text{N}$ in BMSCNC is much lower than that of TMSCNC and CNC, probably arising from the decomposition or incomplete polymerization of structural units,⁴² indicating that BMSCNC possesses superior structural order over other samples.³⁶ Raman spectra were also collected to investigate the microstructure of composites (Figure 3C). The characteristic peaks at 667 cm^{-1} that are ascribed to the breathing modes of triazine rings of C_3N_4 ⁴³ are weakened for the molten salt-

treated samples and even disappear within BMSCNC, further demonstrating the higher structural ordering and crystallinity of the C_3N_4 component in BMSCNC.³⁹ Moreover, the intensity ratio of D- and G-band (I_D/I_G) values of BMSCNC, TMSCNC, and CNC are 1.10 versus 1.04 versus 1.01, respectively, indicating the formation of more defects within the carbon of BMSCNC. It is expected that the rich defects can provide sufficient adsorption sites for Na^+ storage.^{44–46}

The chemical state and composition of BMSCNC, TMSCNC, and CNC (Tables S2 and S3) were studied by X-ray photoelectron spectroscopy (XPS), and only C, N, O were observed without any other impurity elements detected (Figures S12 and S13). In C 1s spectra

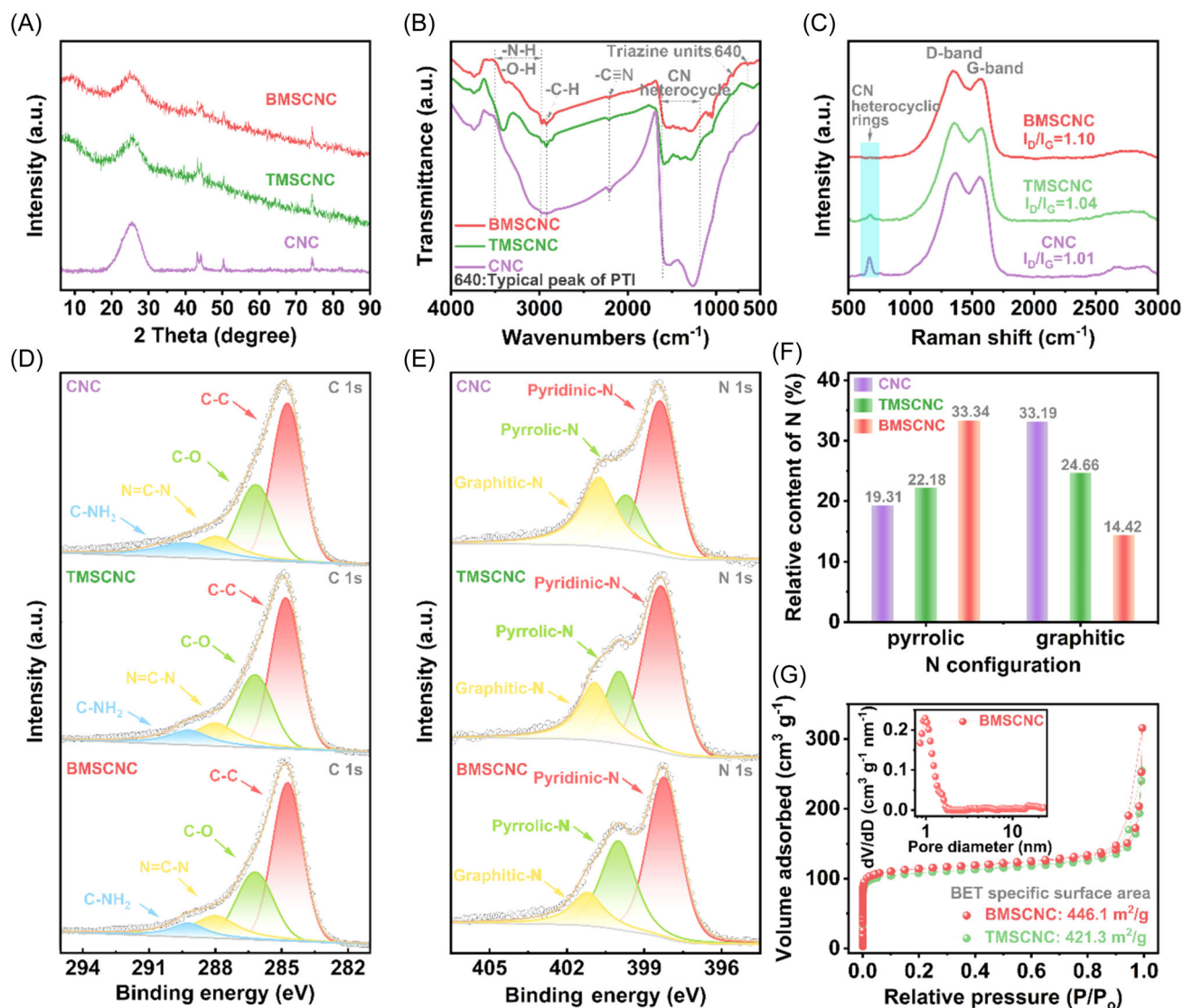


FIGURE 3 Structural characterization. (A) XRD patterns, (B) FT-IR spectra, and (C) Raman spectra of CNC, TMSCNC, and BMSCNC. High-resolution XPS spectra of (D) C 1s and (E) N 1s with (F) the proportion of N configurations within CNC, TMSCNC, and BMSCNC. (G) N₂ adsorption/desorption isotherms and pore size distribution of TMSCNC and BMSCNC.

(Figure 3D), the relative percentage of C-NH₂ produced by the uncondensed amino group of C₃N₄ in BMSCNC was lower than that of TMSCNC and CNC, which further confirms the high polymerization degree of C₃N₄ in BMSCNC.^{47,48} For high-resolution N 1s spectra, the relative contents of deconvoluted pyridinic-N, pyrrolic-N, and graphitic-N in CNC, TMSCNC, and BMSCNC samples were 47.50%/53.16%/52.23%, 19.31%/22.18%/33.35%, and 33.19%/24.66%/14.42% of total N contents (Figure 3E), respectively. Interestingly, the percentage of pyridinic-N was similar in the three samples while the contents of pyrrolic-N gradually increased and graphitic-N decreased from CNC to TMSCNC and then BMSCNC (Figure 3F). It is reported that pyrrolic-N is favorable for Na⁺ storage and

reduction of irreversible reactions while graphitic N species can destroy the crystallinity of C₃N₄ and lead to poor electrochemical performances.^{17,49} In other words, high content of pyrrolic-N with minimum graphitic-N is viewed as a key solution to improve the performance of C₃N₄-based materials for metal ion storage. The unique N configurations shown in this case, therefore, set the foundation for BMSCNC to achieve high electrochemical performances. The nearly overlapping nitrogen adsorption-desorption isotherms revealed a similar surface area of TMSCNC and BMSCNC (421.3 vs. 446.1 m² g⁻¹) while both their pores were primarily micropores with ~1 nm except that the mesopore contribution was slightly higher within BMSCNC (Figures 3G and S14, Table S1).

2.3 | Electrochemical performance characterization and structure-evolution analysis

The coin-type half-cell configuration was used to evaluate the Na^+ storage capability of samples. Galvanostatic charge/discharge (GCD) profiles of BMSCNC at different cycles with operation windows of 0.01–3 V were presented in Figure 4A. The initial capacity loss was ascribed to the irreversible formation of solid electrolyte interphase (SEI) layer,⁵⁰ and the curves at subsequent cycles nearly overlapped with high Coulomb efficiency (>99%) achieved, confirming the great reversibility of

BMSCNC during cycling. The corresponding cycling analysis showed BMSCNC even presented a gradual increase trend of capacity through electrode activation and delivered a reversible capacity of 317.2 mAh g^{-1} after 500 cycles (Figure 4B). Meanwhile, BMSCNC also exhibited reverse capacity growth at 0.1, 0.5, and 1.0 A g^{-1} , as illustrated in Figure S15. In comparison, the CNC and TMSCNC electrodes only showed capacities of 146.7 and 209.1 mAh g^{-1} with capacity retention rates of 76.2% and 90.1%, respectively. BMSCNC also presented superior rate capabilities to its counterparts with the reversible capacities of 338.0, 298.2, 274.9, 243.9, and 193.3 mAh g^{-1} delivered at 0.1, 0.2, 0.5, 1, and 2 A g^{-1} ,

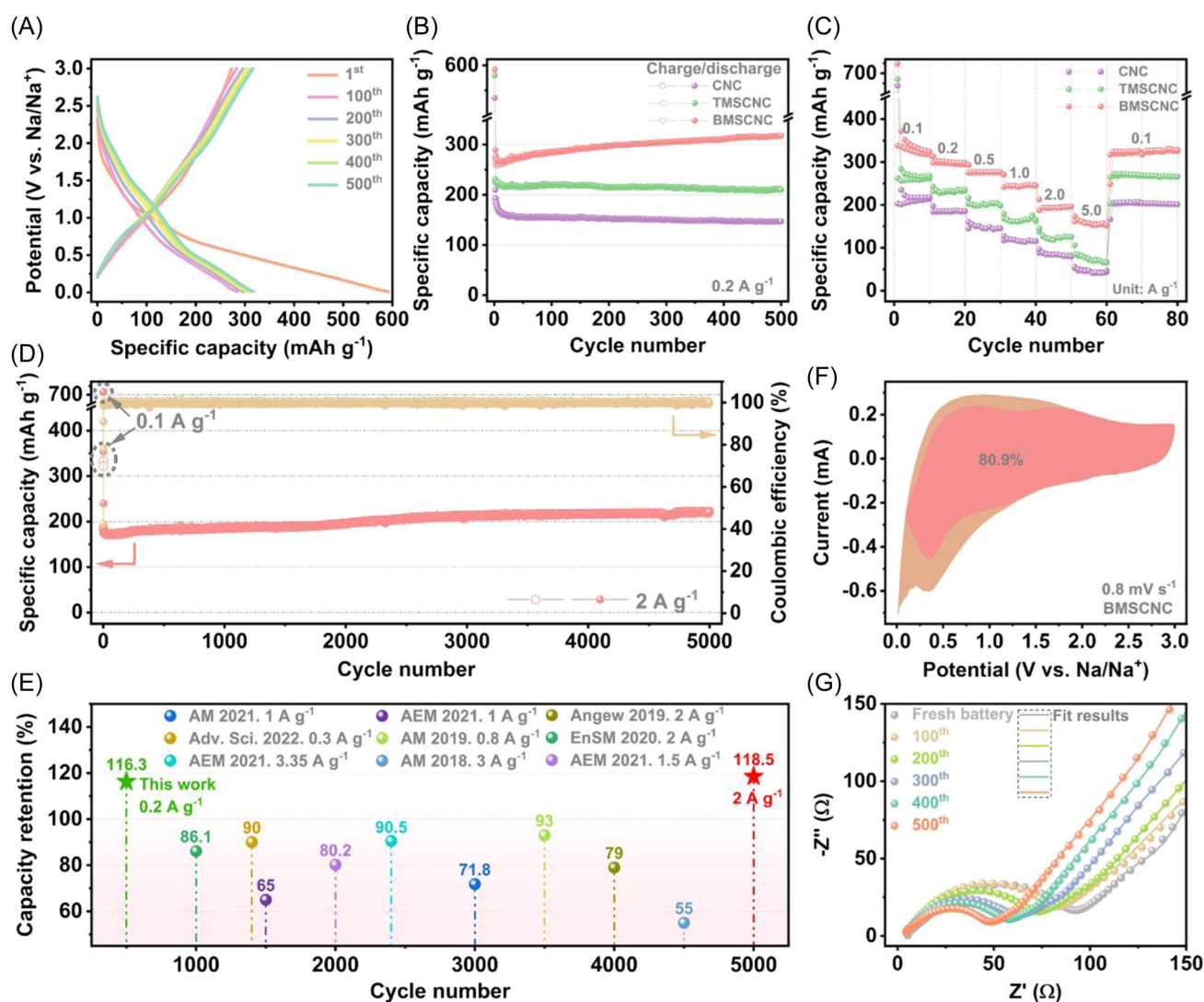


FIGURE 4 Electrochemical performances in half-cell. (A) Galvanostatic charge/discharge profiles of BMSCNC at 0.2 A g^{-1} . (B) Cycling performances of CNC, TMSCNC, and BMSCNC at 0.2 A g^{-1} . (C) Rate capabilities of CNC, TMSCNC, and BMSCNC from 0.1 to 5 A g^{-1} . (D) Long-term cycling performances up to 5000 cycles of BMSCNC at a current density of 2 A g^{-1} with preactivation at 0.1 A g^{-1} for initial two-cycle. (E) Electrochemical performance comparison of this work with reported carbonaceous anode materials for sodium-ion battery. (F) Capacitive contribution in the charge storage of BMSCNC at a sweep rate of 0.8 mV s^{-1} . (G) Nyquist plots of BMSCNC electrodes with fresh and cycled batteries at 0.2 A g^{-1} (100–500 cycles).

respectively (Figure 4C). The electrode can still maintain a high capacity of 161.4 mAh g^{-1} even at the high current density of 5 A g^{-1} , which is higher than most of the reported carbonaceous SIBs anodes.^{51–53} When the current density returns to 0.1 A g^{-1} , the capacity can still be rebounded back to 325.0 mAh g^{-1} , demonstrating the high-rate capability of BMSCNC. Correspondingly, CNC and TMSCNC showed lower capacities of 202.8/262, 183.5/231.4, 144.6/202.2, 116.9/167.7, 87.9/126.6, and $51.9/85 \text{ mAh g}^{-1}$ at current densities of 0.1, 0.2, 0.5, 1, 2, and 5 A g^{-1} , respectively. The long-term cycling performance of BMSCNC was presented in Figure 4D. The capacity-increasing trend through electrode activation can still be observed even within 5000 discharging/charging cycles. After 5000 cycles, BMSCNC can present the reversible capacity of 221.2 mAh g^{-1} with a capacity retention of 118.5%, demonstrating its excellent structural stability during cycling. Additionally, BMSCNC still showed excellent cyclic stability at 2 A g^{-1} without low current preactivation (Figure S16). The postcycling capacities of state-of-the-art carbonaceous anodes were listed in Figures 4E, S17, and Table S4, for comparison. To the best of our knowledge, this result surpasses most of the reported carbonaceous works and is among the record values in all reported carbon-related anodes.

To reveal the kinetic process of as-prepared electrodes, the initial five cyclic voltammetry (CV) measurements on BMSCNC were recorded in a voltage window of 0.01–3 V at 0.1 mV s^{-1} (Figure S18). The highly overlapping curves at the 2–5th cycles further indicate the great reversibility of BMSCNC. The detailed kinetics mechanism of CNC, TMSCNC, and BMSCNC was analyzed by CV curves at different scan rates from 0.1 to 1.0 mV s^{-1} (Figures S19A–S21A). All samples showed similar capacitive-controlled sodium-ion storage mechanism (Figures S19B–S21B) and the capacitive charge contributions of CNC, TMSCNC, and BMSCNC were 65.2%, 74.3%, and 80.9% at the scanning rate of 0.8 mV s^{-1} , respectively (Figures S22 and 4F). Among all samples, BMSCNC showed the highest capacitive contribution and this contribution also increases with the scan rate (Figure S23), which endows the electrode materials with high reversible capacities and excellent rate capability.^{54,55} The electrochemical impedance spectroscopy (EIS) of electrodes in the frequency range of 0.01–100 kHz was also studied with Nyquist plots (Figure S24A) to investigate the transport kinetics of electrons and ions. All Nyquist plots are composed of semicircles from the high- to the medium-frequency region and straight lines in the low-frequency region, corresponding to SEI layer resistance (R_{SEI}), charge transfer resistance (R_{ct}), and Warburg impedance (Z_{w}) related to Na^+ diffusion, respectively. As expected, the R_{ct} value of BMSCNC electrode (81.13Ω)

was much lower than those of TMSCNC (640Ω) and CNC (1146Ω), demonstrating the fast electronic transport kinetics within BMSCNC for rapid Na^+ storage. Furthermore, the diffusion coefficient of sodium ions (D_{Na^+}) of BMSCNC calculated based on the EIS spectra is 1.12×10^{-12} (Figure S24B) which is significantly higher than those of CNC (5.99×10^{-13}) and TMSCNC (7.26×10^{-13}) (Table S5), demonstrating the fastest Na^+ diffusion process within BMSCNC. To reveal the influence of PTI crystalline structure and pyrrolic-N on the charge transfer kinetics, EIS spectra were also collected for BMSCNC at different cycles (Figure 4G). The fitted R_{ct} values decreased continuously during cycling, indicating that the charge transfer kinetics increased gradually through electrode activation. Meanwhile, the σ values also reduced from fresh state to 500th cycles with D_{Na^+} values increased (Figure S25 and Table S6), which explains the unusual capacity growth observed during the long-term cycling in Figure 4B,D.

To probe into the microstructural evolution of electrodes through cycling and investigate the interfacial changes of electrode/electrolyte, the surface morphologies of active materials before and after 5000 cycles were compared with SEM images at different magnifications (Figure 5A–L). It can be clearly observed from the low-magnification SEM images (Figure 5A,C,E,G,I,K) that the surface of BMSCNC electrode was still smooth with structural integrity well maintained even after long-term cycling at 2 A g^{-1} (Figure 5K). In contrast, apparent cracks can be observed on CNC (Figure 5C) and TMSCNC (Figure 5G) electrodes, confirming the robust structure of BMSCNC with high mechanical stability to accommodate the internal stress induced by giant volume swelling during cycling.^{56,57} Further insights into the microstructure with high-magnified SEM images demonstrate the formation of uneven and heterogeneous surfaces within CNC (Figure 5D) and TMSCNC (Figure 5H), which demonstrates that the SEI layer has encountered structural degradation and integrity breaking. It is inferred that with the further breaking of SEI layer, the newly exposed surface continues to react with electrolyte for forming the new layers, which induces the ceaseless consumption of sodium ions/electrolytes and therefore results in the performance fading.^{58–60} Interestingly, the surface of BMSCNC changes from the coarse structure in the pristine sample to dense and uniform leaf-like three-dimensional nanosheets covered on the surface (the cross-sectional images in insets of Figure 5K,L) after long-term cycling. Different from the commonly observed bulk and cracked surfaces as shown in Figure 5D,H, this unique leaf-like nanostructure is more favorable for facilitating the electrolyte penetration/ Na^+ diffusion and minimizing the surface energy

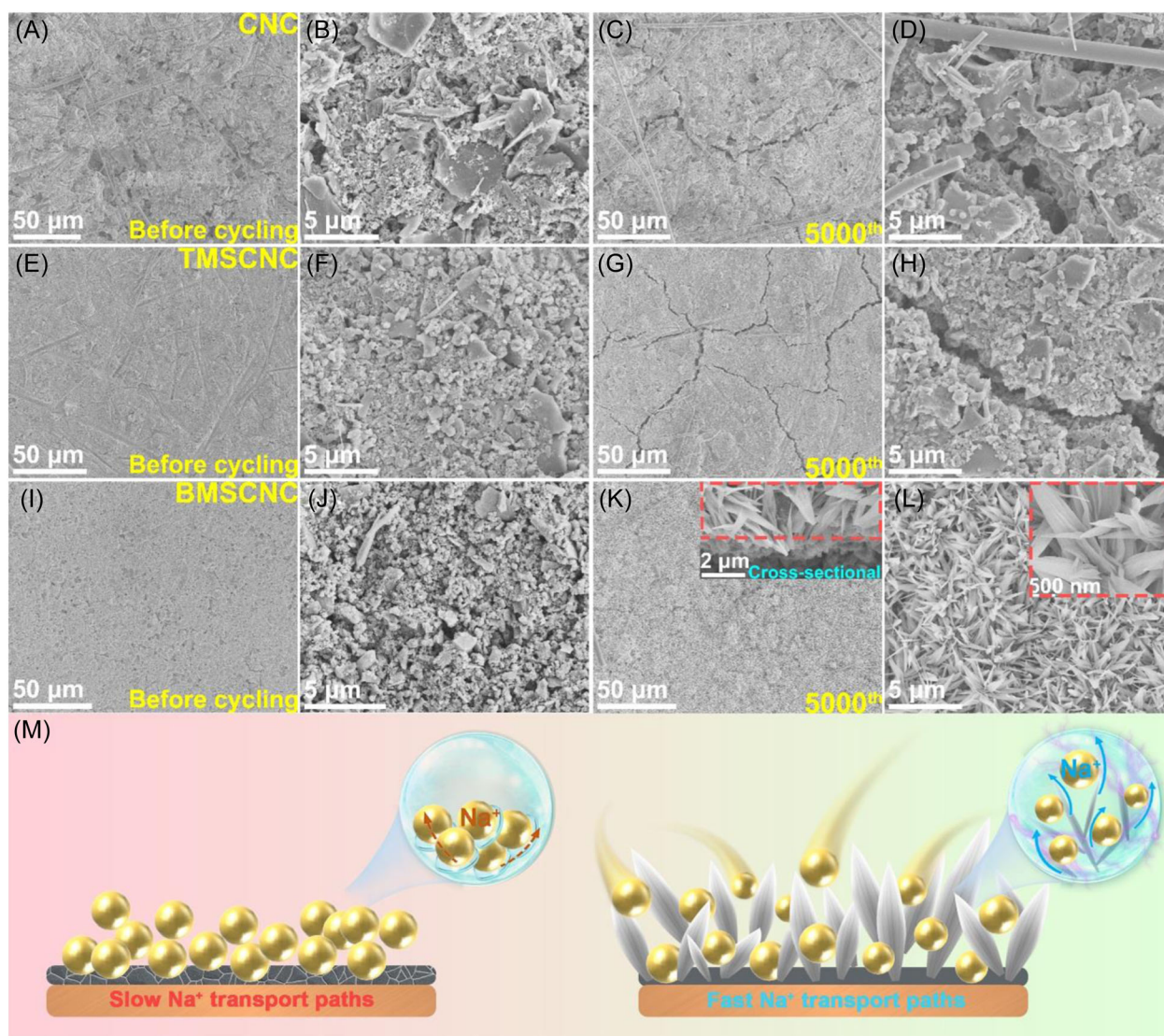


FIGURE 5 Electrode morphology evolution at initial state and after 5000 cycles: (A–D) CNC, (E–H) TMSCNC, and (I–L) BMSCNC (with the cross-section and high-magnification images shown in the inset). (M) Schematic diagram of the electrode morphological evolution.

with reduced internal strain during sodiation/desodiation, which may provide a clue for explaining the robust structure of BMSCNC during electrochemical reactions and its outstanding cycling performance among carbon-based SIBs anodes. A detailed schematic to showcase the surface structure evolution through cycling is presented in Figure 5M.

In view of the excellent performances of BMSCNC electrode in half-cell configurations, the full-cell was also assembled for further evaluation with commercial $\text{Na}_3\text{V}_2(\text{PO}_4)_3$ (NVP) used as the cathode (denoted as BMSCNC//NVP) (Figure 6A). To prevent side reactions in the electrode/electrolyte and minimize the irreversible capacity loss,^{61,62} the BMSCNC anode was presodiated for three cycles with a Na-chip counter electrode at a current density of 0.1 A g^{-1} before testing. As indicated in

Figure 6B, BMSCNC//NVP full cell exhibited a high-rate performance with the reversible capacities of 406.7, 309.4, 250.7, 205.2, 154 mAh g^{-1} achieved, respectively, at 0.1, 0.2, 0.5, 1.0, and 2.0 A g^{-1} , and the capacity can be returned back to 273.6 mAh g^{-1} when the current density was restored to 0.1 A g^{-1} after 20 cycles. Furthermore, its GCD curves at different current densities also showed the similar shape without distortion even at high current density, demonstrating its excellent structural stability during charging/discharging (Figure 6C). The cycling performance of the full-cell also confirmed the robust structure of electrode materials and it can deliver a reversible capacity of 180.6 mAh g^{-1} for 300 cycles at 1 A g^{-1} with a capacity decay of only 0.079% per cycle (Figure 6D). This value has been over most reported for high-performance SIBs and is among the most

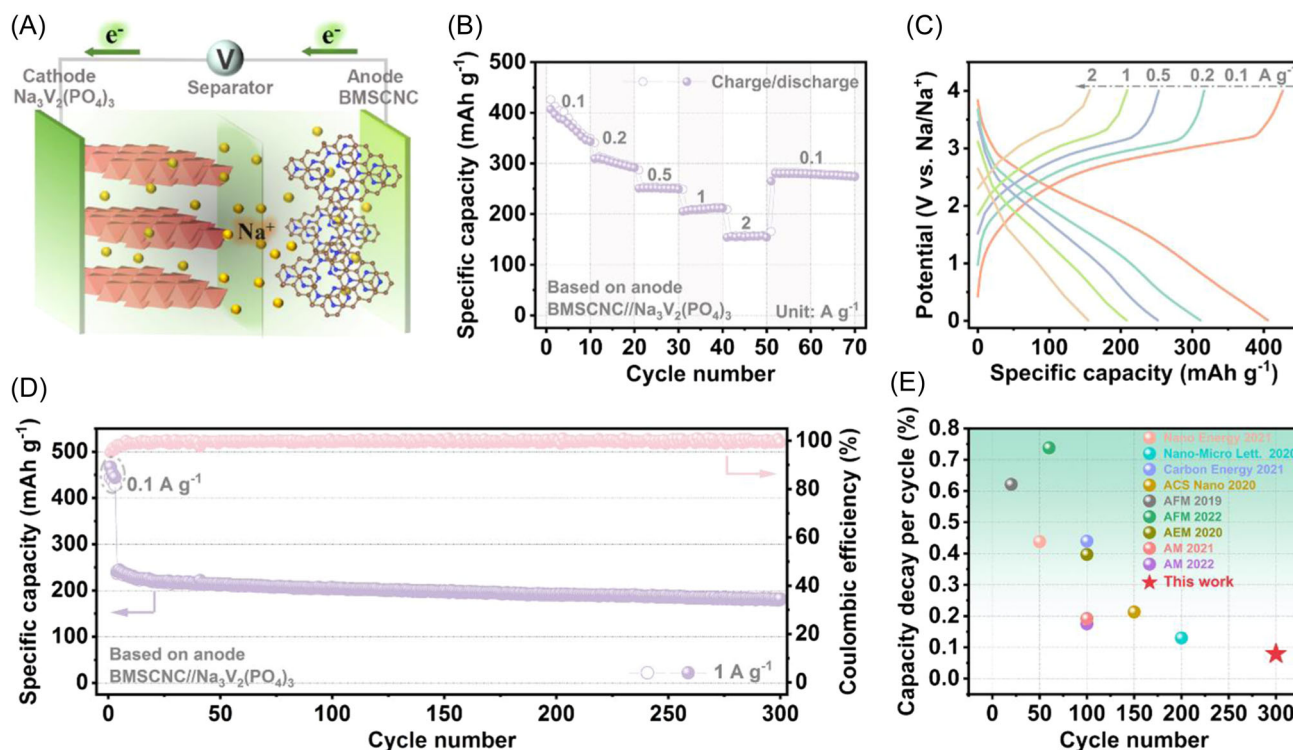


FIGURE 6 Electrochemical performances of BMSCNC//Na₃V₂(PO₄)₃ full cell. (A) Schematic illustration of full cell assembled with BMSCNC as the anode and commercial-grade Na₃V₂(PO₄)₃ as the cathode. (B) Rate capability, (C) GCD curves, and (D) cycling performance at 1 A g⁻¹ of the battery. (E) The comparison of capacity decay per cycle of this work with the SIBs batteries reported in past 3 years.

stabilized full-cell configurations for Na⁺ storage (Figure 6E and Table S7). Note that the cathode material NVP used herein is commercial-grade and the electrochemical performances of the full cell still have substantial improvement spaces by cathode optimization. Meanwhile, it is worth mentioning that the anode material shown here is all-carbon based and its performances far exceed the commercial hard carbon-related anodes. Moreover, its development also does not rely on the distribution of metallic mineral resources and geographical factors that some promising commercial metallic compounds (e.g., Mo₂S) always encounter. Therefore, the material shown in this work may be a promising anode candidate for the commercialization and rapid promotion of SIBs.

3 | CONCLUSION

In summary, a new all-carbon composite (BMSCNC) composed of the crystalline C₃N₄ allotrope PTI and NC was successfully synthesized by the molten salt strategy. By selecting the binary salt LiCl/KCl with low eutectic temperature and high mobility, the polymerization of C₃N₄ as well as the N configuration of the composites was elaborately controlled with the formation of

directional tubular structure assembled by nanosheets. High pyrrolic-N content with minimized graphitic-N was achieved. DFT calculations reveal that the introduction of pyrrolic-N can facilitate the Na⁺ adsorption and significantly enhance the electronic conductivity of the composites. As the anode material for SIBs, the as-prepared BMSCNC composite exhibited high sodium storage capability of 221.2 mAh g⁻¹ with inverse capacity growth of 118.5% at 2 A g⁻¹ after 5000 cycles. This ultra-long-term cycling performance is among the highest values for the reported SIB carbonaceous anodes. Furthermore, the assembled full cell showed a low-capacity decay of only 0.079% per cycle at 1 A g⁻¹ for 300 cycles. This work provides insights into the design and fabrication of high-performance carbon anodes and extends the use of C₃N₄ for broad energy storage applications.

ACKNOWLEDGMENTS

This work was supported by the National Natural Science Foundation of China (51904059), Applied Basic Research Program of Liaoning (2022JH2/101300200), Guangdong Basic and Applied Basic Research Foundation (2022A1515140188), Fundamental Research Funds for the Central Universities (N2002005, N2125004, N2225044). The authors also

appreciate the instrumental analysis from the Analytical and Testing Center, Northeastern University.

CONFLICT OF INTEREST STATEMENT

The authors declare that there are no conflict of interests.

ORCID

Li Li  <http://orcid.org/0000-0003-2308-916X>

REFERENCES

- Gao G, Yang S, Wang S, Li L. Construction of 3D porous MXene supercapacitor electrode through a dual-step freezing strategy. *Scr Mater.* 2022;213:114605.
- Li H, Di S, Niu P, Wang S, Wang J, Li L. A durable half-metallic diatomic catalyst for efficient oxygen reduction. *Energy Environ Sci.* 2022;15(4):1601-1610.
- Sun Z, Zhu K, Liu P, Chen X, Li H, Jiao L. Fluorination treatment of conjugated protonated polyanilines for high-performance sodium dual-ion batteries. *Angew Chem Int Ed.* 2022;61(42):e202211866.
- Liu H, Cai X, Zhi X, et al. An amorphous anode for proton battery. *Nano-Micro Lett.* 2022;15(1):24.
- Sun Z, Zhu K, Liu P, Li H, Jiao L. Optimized cathode for high-energy sodium-ion based dual-ion full battery with fast kinetics. *Adv Funct Mater.* 2021;31(51):2107830.
- Wang Y, Li H, Chen S, et al. An ultralong-life SnS-based anode through phosphate-induced structural regulation for high-performance sodium ion batteries. *Sci Bull.* 2022;67(20):2085-2095.
- Zheng C, Ji D, Yao Q, et al. Electrostatic shielding boosts electrochemical performance of alloy-type anode materials of sodium-ion batteries. *Angew Chem Int Ed.* 2023;62(14):e202214258.
- Tang J, Peng X, Lin T, Huang X, Luo B, Wang L. Confining ultrafine tin monophosphide in $\text{Ti}_3\text{C}_2\text{T}_x$ interlayers for rapid and stable sodium ion storage. *eScience.* 2021;1(2):203-211.
- Wen Y, He K, Zhu Y, et al. Expanded graphite as superior anode for sodium-ion batteries. *Nat Commun.* 2014;5:4033.
- Bai Q, Yang L, Chen H, Mo Y. Computational studies of electrode materials in sodium-ion batteries. *Adv Energy Mater.* 2018;8(17):1702998.
- Ni D, Sun W, Wang Z, et al. Heteroatom-doped mesoporous hollow carbon spheres for fast sodium storage with an ultralong cycle life. *Adv Energy Mater.* 2019;9(19):1900036.
- Pan J, Sun Y, Yan Y, et al. Revisit electrolyte chemistry of hard carbon in ether for Na storage. *JACS Au.* 2021;1(8):1208-1216.
- Zhai B, Li H, Gao G, et al. A crystalline carbon nitride based near-infrared active photocatalyst. *Adv Funct Mater.* 2022;32(47):2207375.
- Wang Y, Liu L, Ma T, Zhang Y, Huang H. 2D graphitic carbon nitride for energy conversion and storage. *Adv Funct Mater.* 2021;31(34):2102540.
- Wang H, Liu X, Niu P, Wang S, Shi J, Li L. Porous two-dimensional materials for photocatalytic and electrocatalytic applications. *Matter.* 2020;2(6):1377-1413.
- Weng G-M, Xie Y, Wang H, et al. A promising carbon/g-C₃N₄ composite negative electrode for a long-life sodium-ion battery. *Angew Chem Int Ed.* 2019;58(39):13727-13733.
- Adekoya D, Gu X, Rudge M, et al. Carbon nitride nanofibres with exceptional lithium storage capacity: from theoretical prediction to experimental implementation. *Adv Funct Mater.* 2018;28(50):1803972.
- Li P, Shen Y, Li X, Huang W, Lu X. Fullerene-intercalated graphitic carbon nitride as a high-performance anode material for sodium-ion batteries. *Energy Environ Mater.* 2022;5(2):608-616.
- Niu P, Li L. Overall photocatalytic water splitting of crystalline carbon nitride with facet engineering. *Chem.* 2020;6(10):2439-2441.
- Niu P, Dai J, Zhi X, Xia Z, Wang S, Li L. Photocatalytic overall water splitting by graphitic carbon nitride. *InfoMat.* 2021;3(9):931-961.
- Li Y, Chen M, Liu B, Zhang Y, Liang X, Xia X. Heteroatom doping: an effective way to boost sodium ion storage. *Adv Energy Mater.* 2020;10(27):2000927.
- Yuan Y, Chen Z, Yu H, et al. Heteroatom-doped carbon-based materials for lithium and sodium ion batteries. *Energy Storage Mater.* 2020;32:65-90.
- Tian L, Li J, Liang F, et al. Molten salt synthesis of tetragonal carbon nitride hollow tubes and their application for removal of pollutants from wastewater. *Appl Catal B.* 2018;225:307-313.
- Diez N, Fuertes AB, Sevilla M. Molten salt strategies towards carbon materials for energy storage and conversion. *Energy Storage Mater.* 2021;38:50-69.
- Zhang D, Guo Y, Zhao Z. Porous defect-modified graphitic carbon nitride via a facile one-step approach with significantly enhanced photocatalytic hydrogen evolution under visible light irradiation. *Appl Catal B.* 2018;226:1-9.
- Ong W-J, Tan L-L, Ng YH, Yong S-T, Chai S-P. Graphitic carbon nitride (g-C₃N₄)-based photocatalysts for artificial photosynthesis and environmental remediation: are we a step closer to achieving sustainability? *Chem Rev.* 2016;116(12):7159-7329.
- Pan Q, Zhang M, Zhang L, et al. FeSe₂@C microrods as a superior long-life and high-rate anode for sodium ion batteries. *ACS Nano.* 2020;14(12):17683-17692.
- Cui Z, He S-A, Liu Q, et al. Graphene-like carbon film wrapped tin (ii) sulfide nanosheet arrays on porous carbon fibers with enhanced electrochemical kinetics as high-performance Li and Na ion battery anodes. *Adv Sci.* 2020;7(18):1903045.
- Wei X, Wang X, Tan X, An Q, Mai L. Nanostructured conversion-type negative electrode materials for low-cost and high-performance sodium-ion batteries. *Adv Funct Mater.* 2018;28(46):1804458.
- Lou S, Zhao Y, Wang J, Yin G, Du C, Sun X. Ti-based oxide anode materials for advanced electrochemical energy storage: lithium/sodium ion batteries and hybrid pseudocapacitors. *Small.* 2019;15(52):1904740.
- Zhang L, Wang W, Lu S, Xiang Y. Carbon anode materials: a detailed comparison between Na-ion and K-ion batteries. *Adv Energy Mater.* 2021;11(11):2003640.
- Zhang W, Yin J, Sun M, et al. Direct pyrolysis of super-molecules: an ultrahigh edge-nitrogen doping strategy of carbon anodes for potassium-ion batteries. *Adv Mater.* 2020;32(25):2000732.

33. Xu Z, Wang J, Guo Z, et al. The role of hydrothermal carbonization in sustainable sodium-ion battery anodes. *Adv Energy Mater.* 2022;12(18):2200208.
34. Kim S, Shirvani-Arani S, Choi S, Cho M, Lee Y. Strongly anchoring polysulfides by hierarchical $\text{Fe}_3\text{O}_4/\text{C}_3\text{N}_4$ nanostructures for advanced lithium-sulfur batteries. *Nano-Micro Lett.* 2020;12(1):139.
35. Li Y, Gong F, Zhou Q, Feng X, Fan J, Xiang Q. Crystalline isotype heptazine/triazine-based carbon nitride heterojunctions for an improved hydrogen evolution. *Appl Catal B.* 2020;268:118381.
36. Guo F, Hu B, Yang C, Zhang J, Hou Y, Wang X. On-surface polymerization of in-plane highly ordered carbon nitride nanosheets toward photocatalytic mineralization of mercaptan gas. *Adv Mater.* 2021;33(42):2101466.
37. Zhang G, Zhu J, Xu Y, et al. In-plane charge transport dominates the overall charge separation and photocatalytic activity in crystalline carbon nitride. *ACS Catal.* 2022;12(8):4648-4658.
38. Xu Y, Fan M, Yang W, et al. Homogeneous carbon/potassium-incorporation strategy for synthesizing red polymeric carbon nitride capable of near-infrared photocatalytic H_2 production. *Adv Mater.* 2021;33(39):2101455.
39. Kang H-J, Lee T-G, Kim H, et al. Thick free-standing electrode based on carbon-carbon nitride microspheres with large mesopores for high-energy-density lithium-sulfur batteries. *Carbon Energy.* 2021;3(3):410-423.
40. Tang Y, Wang X, Chen J, Wang X, Wang D, Mao Z. PVP-assisted synthesis of g- C_3N_4 -derived N-doped graphene with tunable interplanar spacing as high-performance lithium/sodium ions battery anodes. *Carbon.* 2021;174:98-109.
41. Jin A, Liu X, Li M, Jia Y, Chen C, Chen X. One-pot ionothermal synthesized carbon nitride heterojunction nanorods for simultaneous photocatalytic reduction and oxidation reactions: synergistic effect and mechanism insight. *ACS Sustainable Chem Eng.* 2019;7(5):5122-5133.
42. Xu Y, He X, Zhong H, Singh DJ, Zhang L, Wang R. Solid salt confinement effect: an effective strategy to fabricate high crystalline polymer carbon nitride for enhanced photocatalytic hydrogen evolution. *Appl Catal B.* 2019;246:349-355.
43. Qian Y, Lai H, Ma J, et al. Molten salt synthesis of KCl-preintercalated C_3N_4 nanosheets with abundant pyridinic-N as a superior anode with 10 K cycles in lithium ion battery. *J Colloid Interface Sci.* 2022;606:537-543.
44. Sun B, Lou S, Zheng W, et al. Synergistic engineering of defects and architecture in $\text{Co}_3\text{O}_4/\text{C}$ nanosheets toward Li/Na ion batteries with enhanced pseudocapacitances. *Nano Energy.* 2020;78:105366.
45. Zhang X, Weng W, Gu H, et al. Versatile preparation of mesoporous single-layered transition-metal sulfide/carbon composites for enhanced sodium storage. *Adv Mater.* 2022;34(2):2104427.
46. Lee K, Lee YJ, Lee MJ, et al. A 3D hierarchical host with enhanced sodiophilicity enabling anode-free sodium-metal batteries. *Adv Mater.* 2022;34(14):2109767.
47. Qu X, Hu S, Bai J, Li P, Lu G, Kang X. Synthesis of band gap-tunable alkali metal modified graphitic carbon nitride with outstanding photocatalytic H_2O_2 production ability via molten salt method. *J Mater Sci Technol.* 2018;34(10):1932-1938.
48. Huang Z, Chen H, Zhao L, et al. In situ inducing electron-donating and electron-withdrawing groups in carbon nitride by one-step NH_4Cl -assisted route: a strategy for high solar hydrogen production efficiency. *Environ Int.* 2019;126:289-297.
49. Mao Y, Duan H, Xu B, et al. Lithium storage in nitrogen-rich mesoporous carbon materials. *Energy Environ Sci.* 2012;5(7):7950-7955.
50. Ma M, Zhang S, Yao Y, et al. Heterostructures of 2D molybdenum dichalcogenide on 2D nitrogen-doped carbon: superior potassium-ion storage and insight into potassium storage mechanism. *Adv Mater.* 2020;32(22):2000958.
51. Sun F, Wang H, Qu Z, et al. Carboxyl-dominant oxygen rich carbon for improved sodium ion storage: synergistic enhancement of adsorption and intercalation mechanisms. *Adv Energy Mater.* 2021;11(1):2002981.
52. Huang S, Yang D, Qiu X, et al. Boosting surface-dominated sodium storage of carbon anode enabled by coupling graphene nanodomains, nitrogen-doping, and nanoarchitecture engineering. *Adv Funct Mater.* 2022;32(33):2203279.
53. Chen H, Sun N, Zhu Q, Soomro RA, Xu B. Microcrystalline hybridization enhanced coal-based carbon anode for advanced sodium-ion batteries. *Adv Sci.* 2022;9(20):2200023.
54. Lim H, Yu S, Choi W, Kim S-O. Hierarchically designed nitrogen-doped MoS_2 /silicon oxycarbide nanoscale heterostructure as high-performance sodium-ion battery anode. *ACS Nano.* 2021;15(4):7409-7420.
55. Mahmood A, Yuan Z, Sui X, et al. Foldable and scrollable graphene paper with tuned interlayer spacing as high areal capacity anodes for sodium-ion batteries. *Energy Storage Mater.* 2021;41:395-403.
56. Ye S, Wang L, Liu F, Shi P, Yu Y. Integration of homogeneous and heterogeneous nucleation growth via 3D alloy framework for stable Na/K metal anode. *eScience.* 2021;1(1):75-82.
57. Zhu Y, Yao Q, Shao R, et al. Microsized gray tin as a high-rate and long-life anode material for advanced sodium-ion batteries. *Nano Lett.* 2022;22(19):7976-7983.
58. Ji L, Gu M, Shao Y, et al. Controlling SEI formation on SnSb-porous carbon nanofibers for improved Na ion storage. *Adv Mater.* 2014;26(18):2901-2908.
59. Xia J-L, Lu A-H, Yu X-F, Li W-C. Rational design of a trifunctional binder for hard carbon anodes showing high initial coulombic efficiency and superior rate capability for sodium-ion batteries. *Adv Funct Mater.* 2021;31(40):2104137.
60. Jin Y, Le PML, Gao P, et al. Low-solvation electrolytes for high-voltage sodium-ion batteries. *Nat Energy.* 2022;7(8):718-725.
61. Yang F, Hong J, Hao J, et al. Ultrathin few-layer GeP nanosheets via lithiation-assisted chemical exfoliation and their application in sodium storage. *Adv Energy Mater.* 2020;10(14):1903826.
62. Li CC, Wang B, Chen D, et al. Topotactic transformation synthesis of 2D ultrathin GeS_2 nanosheets toward high-rate

and high-energy-density sodium-ion half/full batteries. *ACS Nano*. 2020;14(1):531-540.

SUPPORTING INFORMATION

Additional supporting information can be found online in the Supporting Information section at the end of this article.

How to cite this article: Wang Y, Li H, Di S, et al. Constructing long-cycling crystalline C_3N_4 -based carbonaceous anodes for sodium-ion battery via N configuration control. *Carbon Energy*. 2023;e388. doi:10.1002/cey2.388